

ACCEPTED MANUSCRIPT

## Laser-induced fabrication of nanoporous monolayer WS<sub>2</sub> membranes

To cite this article before publication: Gopinath Danda *et al* 2018 *2D Mater.* in press <https://doi.org/10.1088/2053-1583/aabb73>

### Manuscript version: Accepted Manuscript

Accepted Manuscript is “the version of the article accepted for publication including all changes made as a result of the peer review process, and which may also include the addition to the article by IOP Publishing of a header, an article ID, a cover sheet and/or an ‘Accepted Manuscript’ watermark, but excluding any other editing, typesetting or other changes made by IOP Publishing and/or its licensors”

This Accepted Manuscript is © 2018 IOP Publishing Ltd.

During the embargo period (the 12 month period from the publication of the Version of Record of this article), the Accepted Manuscript is fully protected by copyright and cannot be reused or reposted elsewhere.

As the Version of Record of this article is going to be / has been published on a subscription basis, this Accepted Manuscript is available for reuse under a CC BY-NC-ND 3.0 licence after the 12 month embargo period.

After the embargo period, everyone is permitted to use copy and redistribute this article for non-commercial purposes only, provided that they adhere to all the terms of the licence <https://creativecommons.org/licenses/by-nc-nd/3.0>

Although reasonable endeavours have been taken to obtain all necessary permissions from third parties to include their copyrighted content within this article, their full citation and copyright line may not be present in this Accepted Manuscript version. Before using any content from this article, please refer to the Version of Record on IOPscience once published for full citation and copyright details, as permissions will likely be required. All third party content is fully copyright protected, unless specifically stated otherwise in the figure caption in the Version of Record.

View the [article online](#) for updates and enhancements.

# Laser-Induced Fabrication of Nanoporous Monolayer WS<sub>2</sub> Membranes

*Gopinath Danda<sup>1,2\*</sup>, Paul Masih Das<sup>1\*</sup>, Marija Drndić<sup>1a</sup>*

<sup>1</sup>Department of Physics and Astronomy, and <sup>2</sup>Department of Electrical and Systems Engineering,  
University of Pennsylvania, Philadelphia, Pennsylvania, 19104, USA

## **Abstract**

Porous transition metal dichalcogenides (TMDs) are promising candidates for a variety of catalytic, purification, and energy storage applications. Despite recent advances, current fabrication techniques face issues concerning scalability and control over sample porosity. By utilizing water-assisted laser irradiation, we present here a new method for the fabrication of micron-scale, atomically-thin nanoporous tungsten disulfide (WS<sub>2</sub>) membranes. The electronic and physical structures of the porous membranes are characterized with photoluminescence (PL) spectroscopy and aberration-corrected scanning transmission electron microscopy (AC-STEM), respectively. With increasing laser irradiation dose, we observe a decay of PL signal, and a relative increase in the trion contribution compared to that of the neutral exciton, suggesting defect-related n-type doping and degradation of the membrane. AC-STEM images show the nucleation of tungsten oxide islands on the membrane, and the formation of triangular defect clusters containing a combination of nanopores and oxide-filled regions, providing insight at the

---

<sup>a</sup> Electronic mail: drndic@physics.upenn.edu

1  
2 atomic level into the photo-oxidation process in TMDs. A linear dependence of the nanoporous  
3 area percentage on the laser irradiation dose over the range of  $10^2$ - $10^5$  W/cm<sup>2</sup> is observed. The  
4 methods proposed here pave the way for the scalable production of nanoporous membranes  
5 through the laser-induced photo-oxidation of WS<sub>2</sub> and other transition metal dichalcogenides.  
6  
7  
8  
9

### 10 11 12 **Keywords** 13

14  
15 Transition metal dichalcogenides, tungsten disulfide, nanopores, nanoporous membranes,  
16 defects, photo-oxidation, laser induced nanopores  
17  
18  
19  
20  
21  
22  
23  
24  
25  
26  
27  
28  
29  
30  
31  
32  
33  
34  
35  
36  
37  
38  
39  
40  
41  
42  
43  
44  
45  
46  
47  
48  
49  
50  
51  
52  
53  
54  
55  
56  
57  
58  
59  
60

## Introduction

Among the family of 2D materials, transition metal dichalcogenides (TMDs) have attracted a lot of attention as potential candidates for photodetection,<sup>1,2</sup> purification,<sup>3,4</sup> energy storage,<sup>5,6</sup> and catalysis applications.<sup>7,8</sup> Building upon the successful paradigm established by porous carbide-derived carbon (CDC) compounds in the latter application, porous TMDs and TMD-CDC hybrids have been heavily explored as possible electrocatalysts,<sup>9</sup> photocatalysts,<sup>1,10</sup> and purification catalysts.<sup>7,8,11</sup> Despite their favorable performance, current fabrication techniques for porous TMDs based on solution-phase synthesis and sol-gel methods are primarily limited to relatively slow and energy-intensive recipes that either offer little to no tunability over sample porosity or fail to produce pore sizes below  $\sim 100$  nm and fully utilize the 2D characteristics of the material.<sup>8,10,12</sup> Similarly, recently-reported methods for fabricating nanoporous molybdenum disulfide ( $\text{MoS}_2$ ) based on ion beam patterning<sup>13</sup> and bottom-up molecular beam epitaxy (MBE)<sup>11</sup> seem promising but require a number of time-consuming processes, often under high-vacuum conditions that raise concerns over scalability. This necessitates the development of a process for the fabrication of TMDs with tunable porosity that is both rapid and scalable.

Owing to their direct semiconducting band gap and strong photoluminescence (PL) signature, monolayer TMDs have been probed for various optoelectronic applications such as phototransistors,<sup>14,15</sup> light-emitting diodes,<sup>16</sup> and solar cells.<sup>17,18</sup> Due to their strong optical absorption, the controlled layer-by-layer thinning of  $\text{MoS}_2$  as well as the patterning of micron-scale holes in tungsten disulfide ( $\text{WS}_2$ ) have also been achieved through laser-induced ablation.<sup>1,19</sup> While the basal plane of monolayer flakes is known to be highly stable, intrinsic defects and edge sites have been shown to provide nucleation sites for this degradation process,<sup>20,21</sup> which is accelerated in the presence of water.<sup>21-23</sup> These laser-induced defects,

1  
2 however, have not been observed at the atomic level and their study can provide more insight  
3  
4 into the degradation process.  
5

6  
7 Here, we demonstrate the controlled water-assisted photo-oxidation of pristine monolayer  
8  
9 WS<sub>2</sub> membranes as a new method for producing nanopores and nanoporous TMDs with tunable  
10  
11 porosity on the time scale of a few seconds. We analyze changes in the material's electronic  
12  
13 structure through PL spectroscopy in addition to quantitatively and qualitatively characterizing  
14  
15 the nature of the resulting porous structure using transmission electron microscopy (TEM) and  
16  
17 electron energy loss spectroscopy (EELS).  
18  
19  
20  
21

## 22 **Methods**

23  
24  
25 Monolayer triangular WS<sub>2</sub> flakes are grown using a chemical vapor deposition (CVD)  
26  
27 technique similar to that demonstrated by Kim *et al.* (2016).<sup>24</sup> We note here that the use of  
28  
29 monolayer WS<sub>2</sub> arises from a combination of its highly-developed CVD growth techniques and  
30  
31 exceptional room temperature PL properties in comparison to other TMDs.<sup>25</sup> Figure 1a shows an  
32  
33 optical image of resulting triangular flakes on a 150 nm-thick SiO<sub>2</sub> substrate. The monolayer  
34  
35 nature of the flakes was confirmed *via* Raman spectroscopy (Figure 1b) with an excitation  
36  
37 wavelength of 532 nm. The Raman spectrum consists of the four primary modes – first-order in-  
38  
39 plane acoustic mode,  $LA(M)$  (175 cm<sup>-1</sup>), second-order in-plane acoustic mode,  $2LA(M)$  (353 cm<sup>-1</sup>),  
40  
41 first-order in-plane optical mode,  $E'(\Gamma)$  (357 cm<sup>-1</sup>), and first-order out-of-plane optical mode,  
42  
43  $A'_1$  (419 cm<sup>-1</sup>) – and their derivative peaks.<sup>26–28</sup> The higher relative intensity of the  $2LA(M)$  to  $A'_1$   
44  
45 mode and the absence of a prominent peak at ~ 310 cm<sup>-1</sup> suggests the monolayer quality of the  
46  
47 flake.<sup>27,29</sup> However, to further verify that our flakes are in fact monolayer, we obtain PL spectra,  
48  
49 as described later in the text. The flakes are transferred onto perforated carbon grids (perforation  
50  
51 diameter ~ 2.5 μm) using a standard PMMA-based KOH wet etch technique. A scanning  
52  
53  
54  
55  
56  
57  
58  
59  
60

1  
2 electron microscope (SEM) image of a WS<sub>2</sub> flake suspended over multiple holes is shown in  
3  
4 Figure 1c. Figure 1d shows a high-angle annular dark-field (HAADF) lattice image of a  
5  
6 suspended region that was obtained in an aberration-corrected scanning transmission electron  
7  
8 microscope (AC-STEM) along with (Figure 1d inset) a selected area electron diffraction (SAED)  
9  
10 pattern.  
11  
12  
13

14  
15 Samples were irradiated with a laser using a custom-built illumination setup, as shown in  
16  
17 Figure 2a. Suspended WS<sub>2</sub> membranes were immersed in deionized (DI) water and located  
18  
19 optically using a 60X water immersion objective lens and an integrated CMOS camera. A green  
20  
21 laser ( $\lambda = 532$  nm,  $P = 5$  mW) was then focused on selected membranes for an irradiation time  
22  
23 ( $t$ )  $\sim 5$  seconds with different laser power densities (*i.e.*, irradiation doses) modulated using a step  
24  
25 variable neutral density (ND) filter. It should be noted here that no rastering of the laser was  
26  
27 performed in this study. DI water provides the necessary oxidizing environment for the photo-  
28  
29 oxidation reaction.<sup>21–23</sup> Due to its higher refractive index in comparison to air, DI water also  
30  
31 allows for a higher numerical aperture (NA) objective lens (spot size = 540 nm), which localizes  
32  
33 the effects of photo-oxidation, thus making it easier to analyze the entire affected area within the  
34  
35 limited field of view of the TEM. It should be noted that use of the dichroic mirror in the setup is  
36  
37 required for image capture by the camera and reduces the laser power reaching the sample. As a  
38  
39 result, laser irradiation dose calculations were performed using power values measured at the  
40  
41 sample stage using a power meter. In our experiments, the laser irradiation dose ( $D$ ) was varied  
42  
43 from  $\sim 10^2$  to  $10^5$  W/cm<sup>2</sup>, which is lower than the dose required for laser-induced thermal  
44  
45 ablation of TMDs (MoS<sub>2</sub>).<sup>19</sup> Multiple membranes ( $n \geq 3$ ) were irradiated for each dose (Figure  
46  
47 S1). Immediately after irradiation, samples were annealed at 250°C for 90 minutes in a Ar/H<sub>2</sub>  
48  
49 environment to reduce hydrocarbon contamination during SEM, STEM, and PL analysis. Based  
50  
51 on HAADF STEM images (Figure S6) and previous reports of annealed nanopores and  
52  
53  
54  
55  
56  
57  
58  
59  
60

nanoporous membranes,<sup>4,20</sup> annealing at these temperatures, well below the decomposition temperatures of TMDs ( $\sim 600\text{-}700^\circ\text{C}$ ),<sup>30</sup> does not change the size of defects. A comparison of SEM images of the samples obtained before and after irradiation revealed varying degrees of photo-degradation of the membranes dependent on laser dose (Figure 2b) and served as a quick check before further spectroscopic and AC-STEM analysis were performed. Control experiments in air did not show the formation or expansion of defects in membranes upon laser irradiation, regardless of the presence of initial defects, even for irradiation times,  $t > 4$  minutes and doses,  $D \sim 10^5 \text{ W/cm}^2$  (Figure S2), strongly suggesting the need of a conducive oxidizing environment and illumination condition for defect expansion at the given dose.<sup>20,21</sup>

## Results and Discussion

To study the effect of laser-induced damage on suspended membranes, we characterize changes in the electronic and physical structure of  $\text{WS}_2$  using a combination of PL spectroscopy and AC-STEM imaging, respectively. Figure 3a shows the PL spectrum of a pristine suspended monolayer  $\text{WS}_2$  membrane. An excitation wavelength of 532 nm (spot size = 940 nm) and incident laser power of  $\sim 50 \mu\text{W}$  were used to prevent unwanted laser-induced degradation during measurements.<sup>19</sup> A strong PL signal is obtained near the direct bandgap value of  $\text{WS}_2$  ( $\sim 2.05 \text{ eV}$ ), which verifies the monolayer quality of our flake.<sup>25</sup> The spectrum is curve-fitted to three Lorentzian components – namely the neutral exciton ( $X_0$ ), the trion ( $X_T$ ) and the defect-related ( $X_D$ ) peaks, which are centered around  $\sim 2.02$ ,  $1.99$  and  $1.88 \text{ eV}$ , respectively.<sup>20,31</sup> The average spectral weight percentages of the  $X_0$ ,  $X_T$  and  $X_D$  peaks were calculated from multiple pristine samples and found to be  $\sim 74\%$ ,  $25\%$  and  $1\%$ , respectively.

Figure 3b shows the normalized PL spectra of the  $\text{WS}_2$  membranes before and after laser irradiation at different doses. The before spectra were taken on pristine  $\text{WS}_2$  membranes in air

1  
2 prior to immersion and laser irradiation in DI water. The spectra indicated as after were also  
3  
4 obtained in air, but after the experiment was completed, *i.e.*, the membranes were immersed in  
5  
6 DI water and exposed to laser irradiation. For the non-laser irradiated case ( $P = 0 \text{ W/cm}^2$ ),  
7  
8 samples were immersed in DI water but not exposed to any laser light. The PL peak shift and  
9  
10 intensity changes before and after irradiation are plotted for several irradiation doses in Figure  
11  
12 3c. The spectral weight percentages of post-irradiation spectra were also calculated and are  
13  
14 plotted in Figure 3d. It was observed that the PL peak redshifts for all irradiation doses and the  
15  
16 shift increases with increasing dose, while the PL intensity decays with higher laser irradiation  
17  
18 doses. The PL shift was calculated at different laser doses averaged over  $> 5$  samples for each  
19  
20 dose. Specifically, the PL redshift was found to be  $5.6 \pm 5.0 \text{ meV}$  and  $5.6 \pm 3.6 \text{ meV}$  for  $P = 0$   
21  
22  $\text{W/cm}^2$  and  $P = 4.80 \times 10^3 \text{ W/cm}^2$ , respectively, which are both smaller than the PL shift for  $P =$   
23  
24  $6.33 \times 10^4 \text{ W/cm}^2$  ( $10.6 \pm 6.2 \text{ meV}$ ). We note that the non-zero PL redshift for  $P = 0 \text{ W/cm}^2$  is  
25  
26 likely due to the formation of a small number of defects due to water exposure under ambient  
27  
28 light, which we verify later using AC-STEM analysis (Figure 4a). Similar averaged PL shifts for  
29  
30  $P = 0 \text{ W/cm}^2$  and  $P = 4.80 \times 10^3 \text{ W/cm}^2$  means that PL shifts are not sensitive to the difference in  
31  
32 the density of defects in non-irradiated samples after water exposure and samples irradiated at  
33  
34 low doses ( $< 10^4 \text{ W/cm}^2$ ) (Figures 4a-b and S1). Furthermore, the relatively large error bars in  
35  
36 the PL shift also imply that the variation in the density of defects at low doses across different  
37  
38 samples is large enough such that the averaged PL shifts are indistinguishable between zero-dose  
39  
40 and low-dose ( $< 10^4 \text{ W/cm}^2$ ) irradiated samples. As the irradiation dose increases ( $P = 6.33 \times 10^4$   
41  
42  $\text{W/cm}^2$ ), the defect density increases as expected, leading to a larger PL redshift. For doses from  
43  
44 0 (pristine) to  $10^4 \text{ W/cm}^2$ , the  $X_T$  contribution increases while the  $X_0$  peak contribution  
45  
46 diminishes. While both peaks decay with increasing laser irradiation dose, a conversion from  
47  
48 neutral to charged exciton emission (n-type doping) is also seen *via* a redshift and broadening of  
49  
50  
51  
52  
53  
54  
55  
56  
57  
58  
59  
60

1  
2 the PL spectra. We note that this is opposite to what was observed in plasma-irradiated WS<sub>2</sub> in  
3  
4 which the  $X_T$  contribution decreased.<sup>31</sup> The  $X_D$  contribution remains negligible (< 10%) for all  
5  
6 laser doses, suggesting a different kind of defect formation compared to electron beam-induced  
7  
8 or plasma-induced defects.<sup>20,31</sup> For higher doses ( $D \sim 10^5$  W/cm<sup>2</sup>), the majority of the membranes  
9  
10 were seen to break (Figures 2b, 4d and S1) and the PL spectra obtained after irradiation are  
11  
12 extremely weak compared to those obtained before irradiation (> 800-fold decay). The direct  
13  
14 dependence of laser-induced effects on the laser power we observe (decay of  $X_0$  and  $X_T$ ) is  
15  
16 similar to what has been observed for WSe<sub>2</sub><sup>22</sup> but contrary to the power independence in the  
17  
18 case of MoS<sub>2</sub>.<sup>21</sup>

19  
20  
21  
22  
23  
24 Defects, substrate effects and chemical doping are known to induce n-type doping of  
25  
26 TMDs.<sup>32-34</sup> We can rule out any substrate effects for our case as we are analyzing only  
27  
28 suspended membranes. Since membranes are annealed after laser irradiation, we also preclude  
29  
30 any doping due to O<sub>2</sub>/H<sub>2</sub>O adsorption.<sup>35,36</sup> While we do observe oxide formation on our flakes  
31  
32 due to DI water exposure (from our AC-STEM analysis as shown in Figures 4, 5 and S1), we do  
33  
34 not see a net PL blueshift or  $X_0$  peak contribution enhancement expected from oxide-induced p-  
35  
36 type doping, shown previously by several studies.<sup>37-39</sup> Defect-induced doping is also known to  
37  
38 reduce exciton lifetime in TMDs which can in turn decrease the PL intensity.<sup>40</sup> This suggests that  
39  
40 while laser-induced defects degrade the membrane, they also introduce defect-induced n-type  
41  
42 doping, which is the dominant doping mechanism, in the membrane. It should be noted that the  
43  
44 relatively large error bars (~60-70%) for dose =  $6.33 \times 10^4$  W/cm<sup>2</sup> in Figure 3c-d indicate a wider  
45  
46 distribution in defect sizes and large defect density in the regime of higher irradiation doses,  
47  
48 which we confirm later using AC-STEM analysis (Figure 5).

49  
50  
51  
52  
53  
54 Bulk properties of laser-irradiated TMD flakes have been studied previously using  
55  
56 spectroscopy, optical microscopy and atomic force microscopy.<sup>21-23,41,42</sup> While monolayer TMDs

1  
2 are known to be more resistant to laser degradation than their few-layer counterparts, the former  
3  
4 was still seen to undergo decay, which was attributed to the presence of intrinsic lattice defects in  
5  
6 the monolayer basal plane.<sup>21,22</sup> Indeed, the introduction of defects in the form of nanopores in  
7  
8 suspended monolayers and subsequent laser irradiation was demonstrated to expand the  
9  
10 nanopore at a controllable rate as a function of laser dose.<sup>20</sup> However, to our knowledge, the  
11  
12 effects of laser irradiation on intact monolayers and the fabrication of laser-induced defects have  
13  
14 not yet been explored at the atomic level. A better understanding of the laser-induced defect  
15  
16 creation would allow for not only better control of the process for scalable applications but also  
17  
18 the manipulation of the properties of TMDs.  
19  
20  
21  
22

23  
24 To observe the effects of laser irradiation on our WS<sub>2</sub> membranes, we characterize the  
25  
26 exposed samples using AC-STEM, which enables structural observations of micron-scale  
27  
28 membranes as well as atomic-scale damage. Representative membranes for laser irradiation  
29  
30 doses of 0, 4.80x10<sup>3</sup>, 6.33x10<sup>4</sup>, and 6.31x10<sup>5</sup> W/cm<sup>2</sup> are shown in Figure 4a-d, with  
31  
32 corresponding AC-STEM images of a single defect outlined in yellow shown underneath. We  
33  
34 note that the term defect is taken here to mean any region of the membrane which does not  
35  
36 contain an intact WS<sub>2</sub> lattice. All the membranes shown were part of the same carbon grid and,  
37  
38 as a result, were subjected to the same pre- and post-processing procedures. Regardless of laser  
39  
40 irradiation dose, all flakes demonstrate the formation of white islands visible in the TEM images  
41  
42 not present initially (Figure S5), which, as discussed later, were determined to be tungsten oxide  
43  
44 (WO<sub>3</sub>) through EELS analysis (Figure 5e). Most of the pristine ( $D = 0$  W/cm<sup>2</sup>) samples are intact  
45  
46 with a few photo-induced triangular defects over a suspended area of  $\sim 5$   $\mu\text{m}^2$  (Figure S1). This  
47  
48 suggests that tungsten oxide islands and a small number of defects form even during water  
49  
50 exposure under ambient light. With increasing laser irradiation dose, the observed defects have  
51  
52 larger areas with a noticeably higher density. At the highest dose ( $D \sim 10^5$  W/cm<sup>2</sup>), the defected  
53  
54  
55  
56  
57  
58  
59  
60

1  
2 area is large enough such that the membrane is structurally weakened and therefore collapses.  
3  
4 Two such membranes irradiated at  $6.31 \times 10^5$  W/cm<sup>2</sup>, one of which did not collapse, are shown in  
5  
6 Figure 4d. Additional images of membranes for each laser irradiation dose can be found in the  
7  
8 Figure S1.  
9

10  
11  
12 In order to better understand both the composition and structure of individual defects in the  
13  
14 nanoporous membranes, we obtain atomic resolution AC-STEM images. Figure 5a shows the  
15  
16 morphology of a typical laser-induced defect ( $D \sim 10^3$  W/cm<sup>2</sup>), outlined in yellow (additional  
17  
18 defects in Figure S4). EELS analysis of the bright islands visible on the irradiated membrane  
19  
20 reveals a peak at an energy loss of 532 eV that corresponds to the oxygen K-edge (Figure 5e).  
21  
22 This peak is only observed in the bright clustered features and not elsewhere on the membrane.  
23  
24 The oxide is also seen to deposit irregularly inside the expanded defect, held together by an  
25  
26 amorphous, carbon-based matrix. Closer observation of defect edges shows the clear  
27  
28 demarcation of the intact WS<sub>2</sub> lattice and the amorphous carbon inside the defect, while no clear  
29  
30 lattice structure is seen in the oxide (Figure 5c-d). We note that unlike molybdenum-based  
31  
32 TMDs, where the absence of molybdenum oxide (MoO<sub>3</sub>) after photo-oxidation experiments was  
33  
34 attributed to dissolution of the oxide in water,<sup>19,21</sup> previous reports on tungsten-based TMDs  
35  
36 using X-ray photoelectron spectroscopy and scanning photoemission microscopy have indicated  
37  
38 the appearance of tungsten oxide oxidation states after laser exposure.<sup>1,22,23,43</sup> This agrees with  
39  
40 our direct observations of oxide islands on the laser-irradiated WS<sub>2</sub> membranes. The amorphous  
41  
42 carbon, which is seen to clog part of the defects, shows up in the EELS background spectrum  
43  
44 (Figure 5e) and is likely the result of the polymer-based transfer process and/or the underlying  
45  
46 perforated carbon film.<sup>28,44-46</sup> Under prolonged electron beam (AC-STEM) exposure, the carbon  
47  
48 contamination is seen to expand until it ultimately clogs the defect entirely (Figure S3). Although  
49  
50 the carbon contamination decreases the total nanoporous area of the membrane, it also reduces  
51  
52  
53  
54  
55  
56  
57  
58  
59  
60

1  
2 the minimum effective hole size to the nanometer scale and gives strength to the suspended  
3 membranes, which can facilitate catalysis applications.  
4  
5

6  
7 We classify regions of the laser-induced defects into two distinct parts: an amorphous carbon-  
8 clogged region and a nanoporous region (Figure 5a). For very large defects (Figure 5b), multiple  
9 disjointed nanopores are present due to interspersed oxide clusters held together by the  
10 amorphous carbon, thus giving a perforated appearance to a single defect (Figure S4). We  
11 quantify the dimensions of the nanopores in the suspended membranes using a thresholding  
12 function in ImageJ and obtain a distribution of the effective nanopore diameter as a function of  
13 laser irradiation dose (Figure 5f). Effective nanopore diameter is taken here to be the diameter of  
14 a single circular nanopore with the same area as the irregularly-shaped nanopore inside the  
15 defect. The smallest defect observed in our samples has an area of  $\sim 300 \text{ nm}^2$  while the minimum  
16 effective nanopore diameter was found to be  $\sim 15 \text{ nm}$ . With increasing laser irradiation dose, an  
17 increase in both the average and maximum effective nanopore diameter is seen. Calculating the  
18 nanoporous area percentage of the exposed membranes results in a linear dependence on the  
19 laser irradiation dose given by the empirical formula:  
20  
21  
22  
23  
24  
25  
26  
27  
28  
29  
30  
31  
32  
33  
34  
35  
36  
37

$$38 \quad \text{Nanoporous area (\%)} = a * D + b \quad (1)$$

39 where  $a = 1.2 \times 10^{-4} \text{ cm}^2/\text{W}$  and  $b = 0.42$  are the fitting parameters (Figure 5g).  
40  
41  
42

43 From our observations, the photo-oxidation mechanism seems to occur in two ways: (i)  
44 formation of oxide islands *via* reaction of water or dissolved oxygen with the  $\text{WS}_2$  lattice and  
45 possible replacement or dislocation of sulfur atoms,<sup>23</sup> and (ii) oxidation and expansion of  
46 intrinsic defects into triangular defect clusters *via* reaction of dissolved oxygen with the dangling  
47 bonds of the defects.<sup>20,21</sup> The oxide that is formed by the latter process clogs the defect held  
48 together by amorphous carbon that is present from the transfer process. If the expanded defect  
49  
50  
51  
52  
53  
54  
55  
56  
57  
58  
59  
60

1 becomes large enough (*i.e.*  $> 300 \text{ nm}^2$ ), the carbon-clogged region collapses and gives rise to  
2 nanopores inside the defect. It should be noted here that based on previous studies using higher  
3 laser powers the observed defects are not expected to be thermally-induced as the maximum  
4 power reaching the membrane was measured and limited to below 2 mW ( $P \sim 1.44 \text{ mW}$ ) during  
5 our irradiation experiments.<sup>22,47,48</sup>

## 14 Conclusion

17 In summary, we demonstrated the first study on the fabrication of atomically-thin  $\text{WS}_2$   
18 membranes with tunable porosity via a photo-oxidation-induced process that avoids many of the  
19 sensitive processing conditions required of other techniques. While no laser-induced defects  
20 were seen in air, an aqueous environment produced defects for laser irradiation doses in the  
21 range  $10^2$ - $10^5 \text{ W/cm}^2$ . We found that the creation of defects leads to the relative lowering of the  
22 concentration of neutral excitons compared to trions (n-type doping), combined with a decrease  
23 in PL peak intensity with increase in irradiation dose due to defect-related degradation. AC-  
24 STEM images of the irradiated membranes show triangular clustered defects, which contain a  
25 combination of nanopores and tungsten oxide islands held together by an amorphous carbon  
26 matrix, which arises due to the PMMA-based sample preparation. The smallest defect size  
27 obtained was  $\sim 300 \text{ nm}^2$ , while the minimum effective diameter of nanopores inside the defect  
28 was  $\sim 15 \text{ nm}$ . Tunable membrane porosity was also realized through a linear dependence of  
29 nanoporous area percentage on the laser irradiation dose, with mechanical collapse of most of the  
30 membranes at doses  $\sim 10^5 \text{ W/cm}^2$ . Combined with computer-controlled, time-resolved laser  
31 rastering in a desired pattern (not used in this study), these observations lay the foundation for  
32 facile and scalable fabrication of TMD nanopores and nanoporous membranes.

## Acknowledgements

Raman/PL and STEM/EELS measurements were performed at the Singh Center for Nanotechnology, University of Pennsylvania. The authors gratefully acknowledge the use of the AC-STEM in the Center for Advanced Materials and Nanotechnology at Lehigh University. We thank Dr. M. Brukman and Dr. D. Yates at the University of Pennsylvania, and Dr. R. Keyse at Lehigh University for their assistance. This work was supported by National Science Foundation (NSF) Grant EFRI 2-DARE (EFRI-1542707).

\*G. Danda and P. Masih Das contributed equally to the work.

## References

1. S. Ma, L. Zeng, L. Tao, C.Y. Tang, H. Yuan, H. Long, P.K. Cheng, Y. Chai, C. Chen, K.H. Fung, X. Zhang, S.P. Lau, and Y.H. Tsang, *Sci. Rep.* **7**, 1 (2017).
2. H. Tan, Y. Fan, Y. Zhou, Q. Chen, W. Xu, and J.H. Warner, *ACS Nano* **10**, 7866 (2016).
3. S.E. Skrabalak and K.S. Suslick, *J. Am. Chem. Soc.* **127**, 9990 (2005).
4. J.P. Thiruraman, K. Fujisawa, G. Danda, P. Masih Das, T. Zhang, A. Bolotsky, N. Perea-López, A. Nicolai, P. Senet, M. Terrones, and M. Drndić, *Nano Lett.* (2018).
5. J.B. Cook, H.S. Kim, Y. Yan, J.S. Ko, S. Robbennolt, B. Dunn, and S.H. Tolbert, *Adv. Energy Mater.* **6**, 1 (2016).
6. T. Stephenson, Z. Li, B. Olsen, and D. Mitlin, *Energy Environ. Sci.* **7**, 209 (2014).
7. Z. Zhang, C. Yue, and J. Hu, *Nano* **12**, 1750116 (2017).
8. K.M. Kwok, S.W.D. Ong, L. Chen, and H.C. Zeng, *ACS Catal.* **8**, 714 (2017).
9. J. Dolinska, A. Chidambaram, W. Adamkiewicz, M. Estili, W. Lisowski, M. Iwan, B. Palys, E.J.R. Sudholter, F. Marken, M. Opallo, and L. Rassaei, *J. Mater. Chem. B* **4**, 1448 (2016).
10. Z. Zhou, Y. Lin, P. Zhang, E. Ashalley, M. Shafa, H. Li, J. Wu, and Z. Wang, *Mater. Lett.* **131**, 122 (2014).
11. X. Zhao, D. Fu, Z. Ding, Y.-Y. Zhang, D. Wan, S.J.R. Tan, Z. Chen, K. Leng, J. Dan, W. Fu, D. Geng, P. Song, Y. Du, T. Venkatesan, S.T. Pantelides, S.J. Pennycook, W. Zhou, and K.P. Loh, *Nano Lett.* **18**, 482 (2017).
12. N. Li, Y. Chai, B. Dong, B. Liu, H. Guo, and C. Liu, *Mater. Lett.* **88**, 112 (2012).
13. D.S. Fox, Y. Zhou, P. Maguire, A. O'Neill, C. Ócoileáin, R. Gatensby, A.M. Glushenkov, T. Tao, G.S. Duesberg, I. V. Shvets, M. Abid, M. Abid, H.C. Wu, Y. Chen, J.N. Coleman, J.F. Donegan, and H. Zhang, *Nano Lett.* **15**, 5307 (2015).

- 1  
2 14. Z. Yin, H. Li, H. Li, L. Jiang, Y. Shi, Y. Sun, G. Lu, Q. Zhang, X. Chen, and H. Zhang,  
3  
4 ACS Nano **6**, 74 (2011).  
5
- 6  
7 15. W.M. Parkin, A. Balan, L. Liang, P. Masih Das, M. Lamparski, C.H. Naylor, J.A.  
8  
9 Rodríguez-Manzo, A.T.C. Johnson, V. Meunier, and M. Drndić, ACS Nano **10**, 4134  
10  
11 (2016).  
12
- 13  
14 16. J.S. Ross, P. Klement, A.M. Jones, N.J. Ghimire, J. Yan, D.G. Mandrus, T. Taniguchi, K.  
15  
16 Watanabe, K. Kitamura, W. Yao, D.H. Cobden, and X. Xu, Nat. Nanotechnol. **9**, 268  
17  
18 (2014).  
19
- 20  
21 17. E. Singh, K.S. Kim, G.Y. Yeom, and H.S. Nalwa, ACS Appl. Mater. Interfaces **9**, 3223  
22  
23 (2017).  
24
- 25  
26 18. G. Kakavelakis, A.E. Del Rio Castillo, V. Pellegrini, A. Ansaldo, P. Tzourmpakis, R.  
27  
28 Brescia, M. Prato, E. Stratakis, E. Kymakis, and F. Bonaccorso, ACS Nano **11**, 3517  
29  
30 (2017).  
31
- 32  
33 19. A. Castellanos-Gomez, M. Barkelid, A.M. Goossens, V.E. Calado, H.S.J. van der Zant,  
34  
35 and G.A. Steele, Nano Lett. **12**, 3187 (2012).  
36
- 37  
38 20. G. Danda, P. Masih Das, Y.-C. Chou, J.T. Mlack, W.M. Parkin, C.H. Naylor, K.  
39  
40 Fujisawa, T. Zhang, L.B. Fulton, M. Terrones, A.T.C. Johnson, and M. Drndić, ACS  
41  
42 Nano **11**, 1937 (2017).  
43
- 44  
45 21. E. Parzinger, B. Miller, B. Blaschke, J.A. Garrido, J.W. Ager, A. Holleitner, and U.  
46  
47 Wurstbauer, ACS Nano **9**, 11302 (2015).  
48
- 49  
50 22. S. Ahn, G. Kim, P.K. Nayak, S.I. Yoon, H. Lim, H.-J. Shin, and H.S. Shin, ACS Nano  
51  
52 **10**, 8973 (2016).  
53
- 54  
55 23. P. Atkin, D.W.M. Lau, Q. Zhang, C. Zheng, K.J. Berean, M.R. Field, J.Z. Ou, I.S. Cole,  
56  
57 T. Daeneke, and K. Kalantar-Zadeh, 2D Mater. **5**, 15013 (2018).  
58  
59  
60

- 1
  - 2
  - 3
  - 4
  - 5
  - 6
  - 7
  - 8
  - 9
  - 10
  - 11
  - 12
  - 13
  - 14
  - 15
  - 16
  - 17
  - 18
  - 19
  - 20
  - 21
  - 22
  - 23
  - 24
  - 25
  - 26
  - 27
  - 28
  - 29
  - 30
  - 31
  - 32
  - 33
  - 34
  - 35
  - 36
  - 37
  - 38
  - 39
  - 40
  - 41
  - 42
  - 43
  - 44
  - 45
  - 46
  - 47
  - 48
  - 49
  - 50
  - 51
  - 52
  - 53
  - 54
  - 55
  - 56
  - 57
  - 58
  - 59
  - 60
24. M.S. Kim, S.J. Yun, Y. Lee, C. Seo, G.H. Han, K.K. Kim, Y.H. Lee, and J. Kim, *ACS Nano* **10**, 2399 (2016).
25. H.R. Gutiérrez, N. Perea-López, A.L. Elías, A. Berkdemir, B. Wang, R. Lv, F. López-Urías, V.H. Crespi, H. Terrones, and M. Terrones, *Nano Lett.* **13**, 3447 (2013).
26. N. Perea-López, A.L. Elías, A. Berkdemir, A. Castro-Beltrán, H.R. Gutiérrez, S. Feng, R. Lv, T. Hayashi, F. López-Urías, S. Ghosh, B. Muchharla, S. Talapatra, H. Terrones, and M. Terrones, *Adv. Funct. Mater.* **23**, 5511 (2013).
27. A. Berkdemir, H.R. Gutiérrez, A.R. Botello-Méndez, N. Perea-López, A.L. Elías, C.-I. Chia, B. Wang, V.H. Crespi, F. López-Urías, J.-C. Charlier, H. Terrones, and M. Terrones, *Sci. Rep.* **3**, 1755 (2013).
28. J.T. Mlack, P. Masih Das, G. Danda, Y.-C. Chou, C.H. Naylor, Z. Lin, N. Perea-López, T. Zhang, M. Terrones, A.T.C. Johnson, and M. Drndić, *Sci. Rep.* **7**, 43037 (2017).
29. W. Zhao, Z. Ghorannevis, K.K. Amara, J.R. Pang, M. Toh, X. Zhang, C. Kloc, P.H. Tan, and G. Eda, *Nanoscale* **5**, 9677 (2013).
30. X. Lu, M.I.B. Utama, J. Zhang, Y. Zhao, and Q. Xiong, *Nanoscale* **5**, 8904 (2013).
31. P.K. Chow, R.B. Jacobs-Gedrim, J. Gao, T.M. Lu, B. Yu, H. Terrones, and N. Koratkar, *ACS Nano* **9**, 1520 (2015).
32. Z. Wu, W. Zhao, J. Jiang, T. Zheng, Y. You, J. Lu, and Z. Ni, *J. Phys. Chem. C* **121**, 12294 (2017).
33. K.F. Mak, K. He, C. Lee, G.H. Lee, J. Hone, T.F. Heinz, and J. Shan, *Nat. Mater.* **12**, 207 (2013).
34. L. Yang, K. Majumdar, H. Liu, Y. Du, H. Wu, M. Hatzistergos, P.Y. Hung, R. Tieckelmann, W. Tsai, C. Hobbs, and P.D. Ye, *Nano Lett.* **14**, 6275 (2014).
35. H. Nan, Z. Wang, W. Wang, Z. Liang, Y. Lu, Q. Chen, D. He, P. Tan, F. Miao, X. Wang,

- 1  
2 J. Wang, and Z. Ni, *ACS Nano* **8**, 5738 (2014).  
3  
4 36. Y. Ma, Y. Dai, M. Guo, C. Niu, J. Lu, and B. Huang, *Phys. Chem. Chem. Phys.* **13**,  
5  
6 15546 (2011).  
7  
8 37. S. McDonnell, A. Azcatl, R. Addou, C. Gong, C. Battaglia, S. Chuang, K. Cho, A. Javey,  
9  
10 and R.M. Wallace, *ACS Nano* **8**, 6265 (2014).  
11  
12 38. M. Yamamoto, S. Dutta, S. Aikawa, S. Nakaharai, K. Wakabayashi, M.S. Fuhrer, K.  
13  
14 Ueno, and K. Tsukagoshi, *Nano Lett.* **15**, 2067 (2015).  
15  
16 39. C. Zhou, Y. Zhao, S. Raju, Y. Wang, Z. Lin, M. Chan, and Y. Chai, *Adv. Funct. Mater.*  
17  
18 **26**, 4223 (2016).  
19  
20 40. Z. Wu, Z. Luo, Y. Shen, W. Zhao, W. Wang, H. Nan, X. Guo, L. Sun, X. Wang, Y. You,  
21  
22 and Z. Ni, *Nano Res.* **9**, 3622 (2016).  
23  
24 41. H. Li, G. Lu, Y. Wang, Z. Yin, C. Cong, Q. He, L. Wang, F. Ding, T. Yu, and H. Zhang,  
25  
26 *Small* **9**, 1974 (2013).  
27  
28 42. J. Gao, B. Li, J. Tan, P. Chow, T.M. Lu, and N. Koratkar, *ACS Nano* **10**, 2628 (2016).  
29  
30 43. J. Lu, J.H. Lu, H. Liu, B. Liu, K.X. Chan, J. Lin, W. Chen, K.P. Loh, and C.H. Sow, *ACS*  
31  
32 *Nano* **8**, 6334 (2014).  
33  
34 44. A. Pirkle, J. Chan, A. Venugopal, D. Hinojos, C.W. Magnuson, S. McDonnell, L.  
35  
36 Colombo, E.M. Vogel, R.S. Ruoff, and R.M. Wallace, *Appl. Phys. Lett.* **99**, 2 (2011).  
37  
38 45. Y.-C. Lin, C.-C. Lu, C.-H. Yeh, C. Jin, K. Suenaga, and P.-W. Chiu, *Nano Lett.* **12**, 414  
39  
40 (2011).  
41  
42 46. C.M. McGilvery, A.E. Goode, M.S.P. Shaffer, and D.W. McComb, *Micron* **43**, 450  
43  
44 (2012).  
45  
46 47. S. Najmaei, Z. Liu, P.M. Ajayan, and J. Lou, *Appl. Phys. Lett.* **100**, 13106 (2012).  
47  
48  
49 48. H. Terrones, E. Del Corro, S. Feng, J.M. Poumirol, D. Rhodes, D. Smirnov, N.R.  
50  
51  
52  
53  
54  
55  
56  
57  
58  
59  
60

1  
2 Pradhan, Z. Lin, M.A.T. Nguyen, A.L. Elías, T.E. Mallouk, L. Balicas, M.A. Pimenta, and  
3  
4 M. Terrones, *Sci. Rep.* **4**, 4215 (2014).  
5  
6  
7  
8  
9  
10  
11  
12  
13  
14  
15  
16  
17  
18  
19  
20  
21  
22  
23  
24  
25  
26  
27  
28  
29  
30  
31  
32  
33  
34  
35  
36  
37  
38  
39  
40  
41  
42  
43  
44  
45  
46  
47  
48  
49  
50  
51  
52  
53  
54  
55  
56  
57  
58  
59  
60

Accepted Manuscript

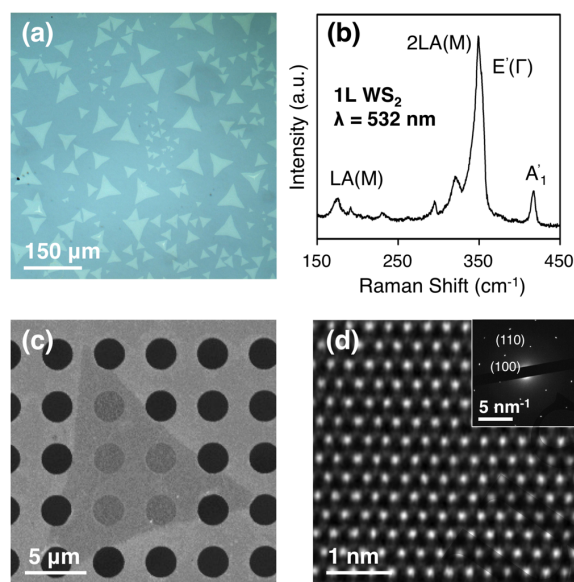


**Figure 1.** (a) Optical image of CVD-grown monolayer WS<sub>2</sub> flakes on SiO<sub>2</sub>. (b) Raman spectra ( $\lambda = 532$  nm) of a monolayer WS<sub>2</sub> flake with indicated primary modes. (c) Scanning electron microscope (SEM) image of a WS<sub>2</sub> flake suspended on a holey carbon grid. Samples such as these were used in PL and photo-oxidation experiments. (d) High-angle annular dark-field (HAADF) aberration-corrected scanning transmission electron microscope (AC-STEM) image of a monolayer WS<sub>2</sub> lattice taken at 80 kV. (inset) Selected area electron diffraction (SAED) pattern along the high-symmetry [001] zone axis showing the (100) and (110) diffraction spots.

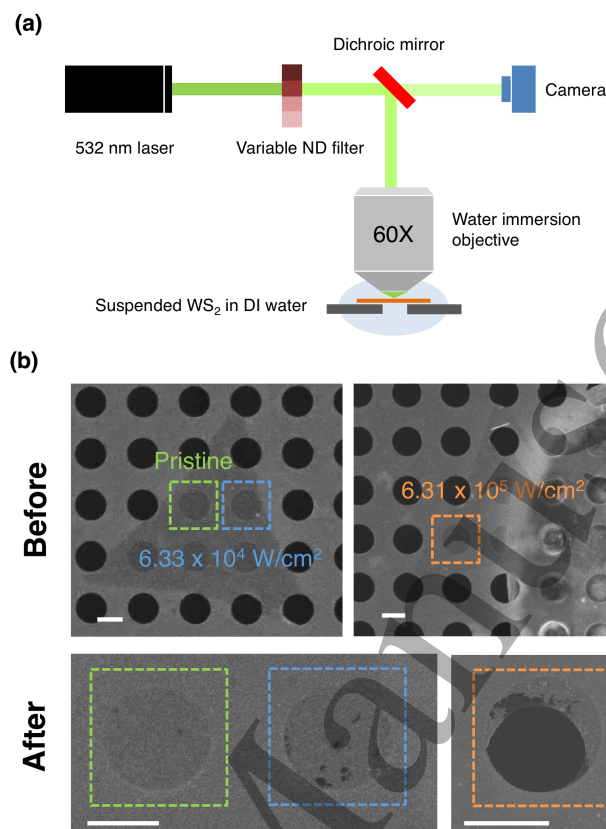


**Figure 2.** (a) Schematic of the laser irradiation setup where the power of the laser ( $\lambda = 532$  nm) is controlled using a step variable neutral density (ND) filter and focused onto the suspended  $\text{WS}_2$  membrane immersed in de-ionized (DI) water using a 60X water immersion objective and an integrated camera. (b) SEM images of monolayer  $\text{WS}_2$  flakes suspended over a holey carbon grid showing photo-oxidation induced damage of a suspended membrane before and after laser irradiation with different doses ( $6.33 \times 10^4$  and  $6.31 \times 10^5$   $\text{W}/\text{cm}^2$ ). A pristine membrane is also shown before and after the experiment. Scale bars are 2  $\mu\text{m}$ .

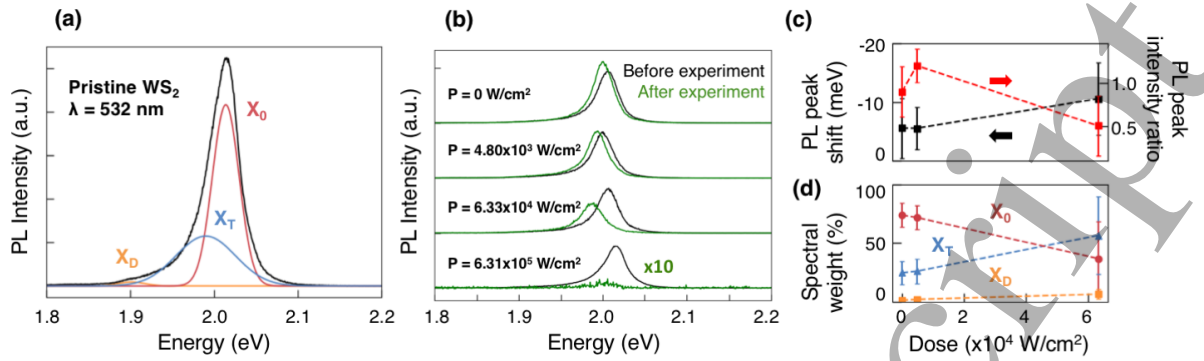


**Figure 3.** (a) Photoluminescence (PL) spectra of a pristine suspended monolayer WS<sub>2</sub> membrane before laser irradiation. The PL spectra was curve-fitted to three spectral components: neutral exciton, X<sub>0</sub> (red), at ~ 2.02 eV, trion, X<sub>T</sub> (blue), at ~ 1.98 eV, and defect, X<sub>D</sub> (orange), ~ 1.88 eV. (b) PL spectra of suspended WS<sub>2</sub> membranes taken in air after being immersed in DI water and exposed (green) to laser irradiation ( $\lambda = 532$  nm) at doses of 0,  $4.80 \times 10^3$ ,  $6.33 \times 10^4$  and  $6.31 \times 10^5$  W/cm<sup>2</sup>, each showing the corresponding spectra before the experiment (black), *i.e.*, prior to immersion and irradiation in DI water. All PL measurements shown here were performed in air. Due to a weak post-experiment PL spectra intensity for  $6.31 \times 10^5$  W/cm<sup>2</sup>, it has been enhanced by a factor of 10. The initial PL peak frequencies of the samples vary between 2.02 and 2.00 eV as the suspended regions are located at different positions over the same flake or are on different flakes. The magnitudes of these initial PL variations across a single sample or different samples are consistent with previous reports.<sup>20,24,25</sup> (c) PL peak shift (black) and intensity ratio (red) before and after irradiation as a function of laser irradiation dose. (d) Spectral weight percentage of each spectral component in the post-experiment PL spectra as a function of laser irradiation dose.

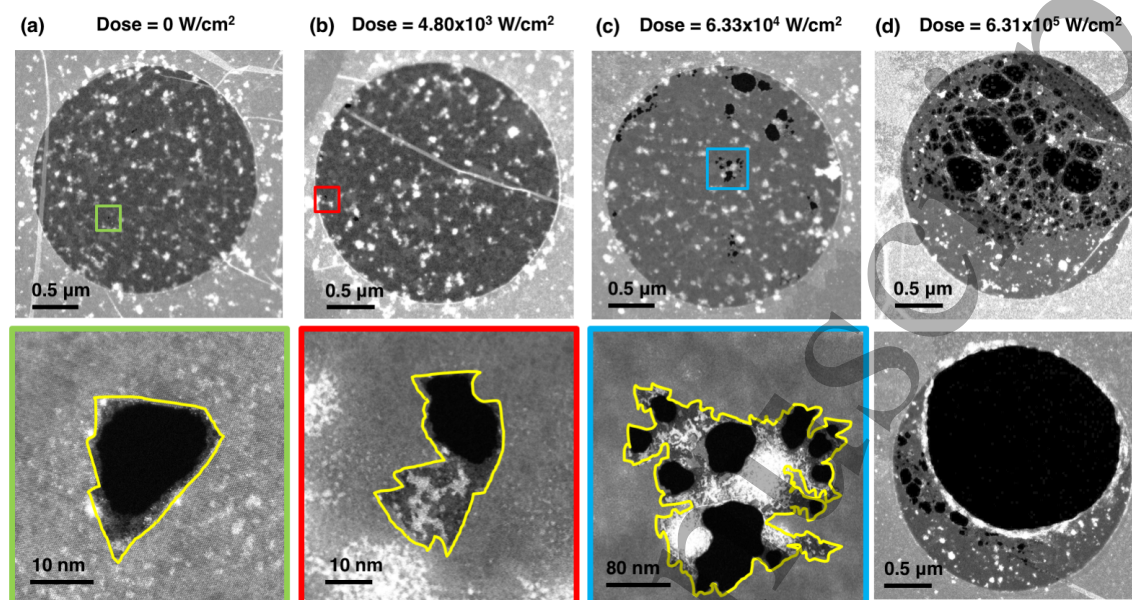


**Figure 4.** (Top row) Low-magnification HAADF AC-STEM images of suspended nanoporous WS<sub>2</sub> membranes after exposure to laser irradiation doses of (a) 0, (b)  $4.80 \times 10^3$ , (c)  $6.33 \times 10^4$ , and (d)  $6.31 \times 10^5$  W/cm<sup>2</sup> with (bottom row) high-magnification images of selected defects. The defect shown for 0 W/cm<sup>2</sup> (green) represents a defect that formed due to photo-oxidation under ambient conditions. The low-magnification image shown for  $6.31 \times 10^5$  W/cm<sup>2</sup> (row (d), top) is one of the few membranes that did not become structurally weakened and (row (d), bottom) one which collapsed at this dose. Additional images of membranes for each laser irradiation dose can be found in the Supplementary Information.

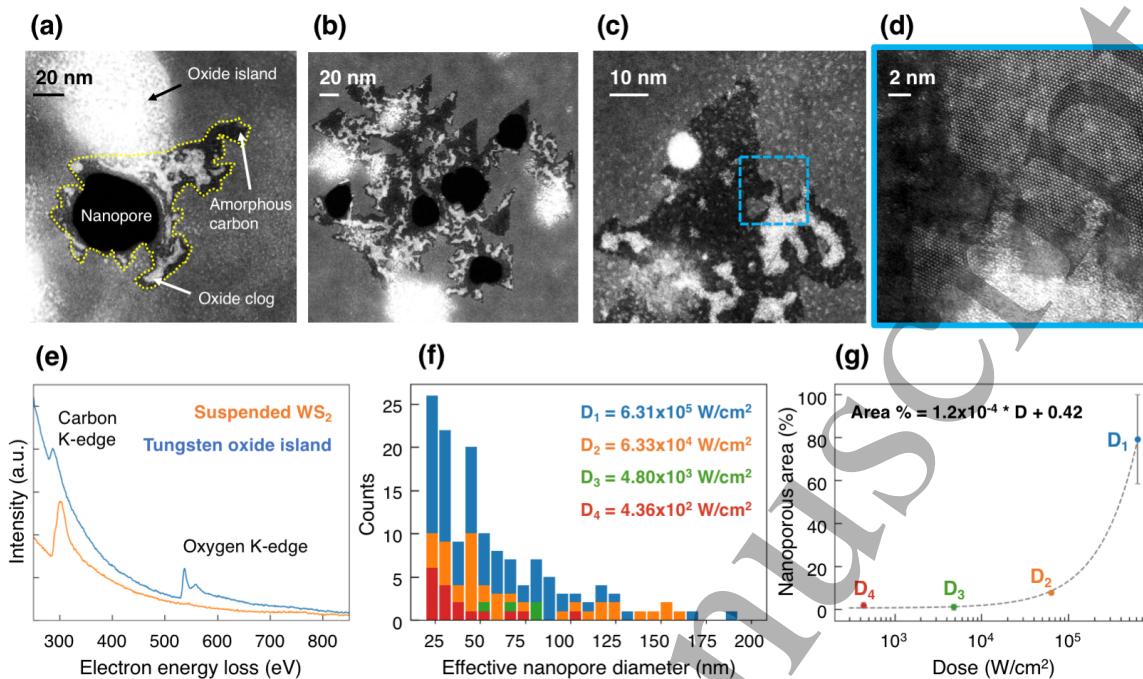


**Figure 5.** (a-b) AC-STEM image of typical photo-oxidation induced defects showing a number of features – (i) defect area (outlined in yellow in a), (ii) nanopore(s) inside the defect, (iii) amorphous carbon-filled part of the defect, (iv) tungsten-oxide-filled part of the defect, and (v) tungsten oxide island in the vicinity of the defect. (c) AC-STEM image of a defect that is fully clogged by amorphous carbon and oxide and (d) a closer view of the edge of the defect showing an intact  $WS_2$  lattice and amorphous nature of the oxide. (e) Electron energy loss spectroscopy (EELS) spectra of the suspended region (orange) and oxide region (blue) from panel (a), exhibiting the oxygen K-edge only in the oxide region. The carbon peak is from hydrocarbon contamination. (f) Effective nanopore diameter distribution for laser irradiation doses of  $4.36 \times 10^2$  (red),  $4.80 \times 10^3$  (green),  $6.33 \times 10^4$  (orange), and  $6.31 \times 10^5$   $W/cm^2$  (blue). (g) Percentage of the total suspended area corresponding to the nanoporous regions as a function of laser irradiation dose with linear fit indicated by the dotted line on linear-logarithmic scale.